Acta metall. Vol. 31, No. 11, pp. 1829–1840, 1983
Printed in Great Britain.

0001-6160/83/ $3.00 + 0.00

MECHANISMS OF HOT-ISOSTATIC PRESSING

F. B. SWINKELS[1,4], D. S. WILKINSON[2], E. ARZT[3] and M. F. ASHBY[4]

[1]School of Mechanical Engineering, New South Wales Institute of Technology, NSW, Australia,
[2]McMaster University, Department of Metallurgy, Canada,
[3]Max-Planck-Institut fur Metallforschung, Stuttgart, F.R.G. and
[4]Cambridge University, Engineering Department, Cambridge, U.K.

(*Received* 17 *April* 1983; *in revised form* 27 *May* 1983)

Abstract—The hot-isostatic pressing of lead, tin and PMMA has been studied, using a rig which enables continuous measurement of density during a test. For the range of experimental conditions used, the dominant mechanisms of densification are plasticity and creep. We found large discrepancies between the data and previous models for these mechanisms. We present improved models, which, while still approximate, include new physical ideas and give a better description of the experiments.

Résumé—Nous avons étudié la compression isostatique à chaud du plomb, de l'étain et d'alliages, en utilisant une installation permettant la mesure continue de la densité au cours d'un essai. Dans les conditions expérimentales utilisées, les mécanismes de densification prépondérants sont la plasticité et le fluage. Nous avons mis en évidence de grandes différences entre les résultats et les modèles antérieurs de ces mécanismes. Nous présentons des modèles améliorés qui, bien qu'encore approchés, renferment des idées physiques nouvelles et donnent une meilleure description des expériences.

Zusammenfassung—Mit einer Einrichtung, die die kontinuierliche Messung der Dichte erlaubt, wurde die Heißextrusion von Blei, Zinn und PMMA untersucht. Plastizität und Kriechen sind vorwiegende Mechanismen bei den benutzten experimentellen Bedingungen. Wir beobachteten große Unterschiede Zwischen den Ergebnissen und früheren Modellen für diese Mechanismen. Verbesserte Modelle werden vorgeschlagen, die zwar näherungsweise sind, jedoch neue physikalische Ansätze enthalten und die Ergebnisse besser beschreiben.

1. INTRODUCTION

The pressureless sintering of an aggregate of powder at high temperature is driven by capillary forces. If, in addition, a pressure is applied, then some of the mechanisms contributing to pressureless sintering are enhanced, and new mechanisms appear. The pressure may, for example, cause rearrangement of the particles [1–3]; it may induce plasticity and creep in the compact [4–8]; and it may augment the effects of surface tension as a driving force for diffusion [9].

Numerous models have been developed for these mechanisms (see reviews [1, 8, 10–13]) and the competing effect of the possible mechanisms has been considered through the development of pressure sintering diagrams [8, 14]. However, critical tests of the theories have been hindered by lack of data. Moreover, where data do exist, they often do not provide an adequate test of the models, for a variety of reasons. First, most models apply to isostatic pressing while most of the data are collected in die-pressing experiments. Second, we require accurate materials data for evaluation of the models. This means that both creep and densification data should be available for the same material.

The work described here is an attempt to improve this situation. It describes a set of experiments on lead, tin and PMMA powders, which use a hot-isostatic press in which density changes can be followed continuously. In addition, creep tests have been performed to provide the required materials data. This report is necessarily brief; more details of the experimental method can be found in the theses of Wilkinson [14] and Swinkels [13].

2. EXPERIMENTAL METHOD

2.1. The press

Figure 1 shows a cross-section of the pressure vessel used for pressing. It consists of two chambers, separated by an inner sleeve containing a moveable piston. The powder is contained in a flexible bag, attached to the top of the inner chamber. A porous plug above the powder allows the bag to be evacuated and purged with gas. The inner chamber is a sealed compartment containing a constant volume of silicone oil. The outer chamber, filled with the same oil, acts as a reservoir. Pressure is applied by a hydraulic pump, and held constant during the test by means of an accumulator. As the powder densifies, the piston separating the two chambers moves upward. Its displacement is measured by strain gauges attached to a cantilever beam, the free end of which slides on a tapered section of the piston stem. By calibrating the output of the strain gauges, the relative density Δ/Δ_0 can be measured continuously. It is given by

$$\frac{\Delta}{\Delta_0} = \frac{\Delta_f}{\Delta_0}\frac{V_f}{V} \qquad (1)$$

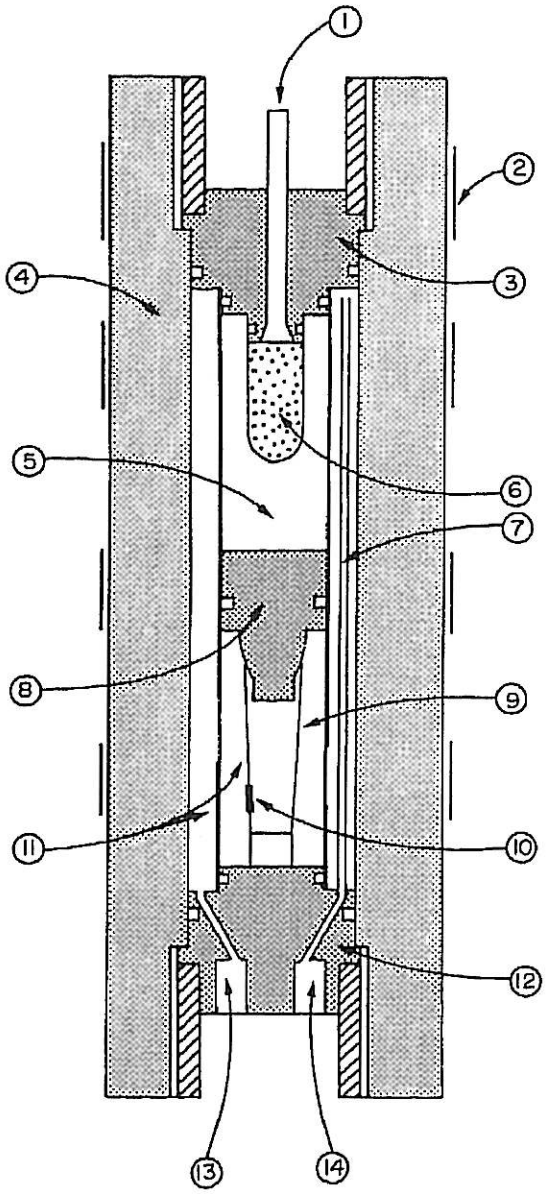

Fig. 1. A cross-sectional view of the hot-isostatic press.

where V and V_f are the current and final volumes respectively (of the chamber). Δ_f is the final density of the compact, and Δ_0 is the density of the material of which the particles are made. Thus Δ/Δ_0 tends to the value 1 as full density is approached.

The vessel is heated by four external resistor bands. The temperature is controlled to ± 0.5°C by a thermocouple situated between the two central bands, and monitored by a second thermocouple close to the specimen. The powder, contained in a bag of rubber, lead or tin (as appropriate) is fixed to the top cap of the press and repeatedly evacuated and purged with hydrogen. The pressure vessel is preheated to the test temperature, the evacuated specimen lowered into the oil and a cover-screw tightened down. Once a stable test temperature has been reached (30 min), when the pressure is applied. It takes about 30 sec to reach the test pressure after which both the temperature and pressure are held constant for the duration of the test (24 h). For all tests, the zero time point is taken when the test pressure is first reached. Reproducibility in density measurements is $\pm 2\%$.

2.2. *Materials*

The temperature limitations of the press required powders with low melting points. We used lead, tin and polymethylmethacrylate (PMMA). The metal powders (Figs 2 and 3) were reduced to a size range of 100–200 μm diameter by sieving. Oxide on the as-received powders was reduced by washing in a solution of 5% acetic acid and 2% hydrogen peroxide in water, (for the lead powder) and 1% HCl in alcohol (for the tin powder), followed by rinsing in alcohol. The powder was dried in a vacuum, then immediately transferred into a bag to minimise further oxidation. After an initial volume measurement, it was placed in the sintering press.

The PMMA powder, after sieving, consisted of almost spherical particles with a diameter range of 50–100 μm (Fig. 4).

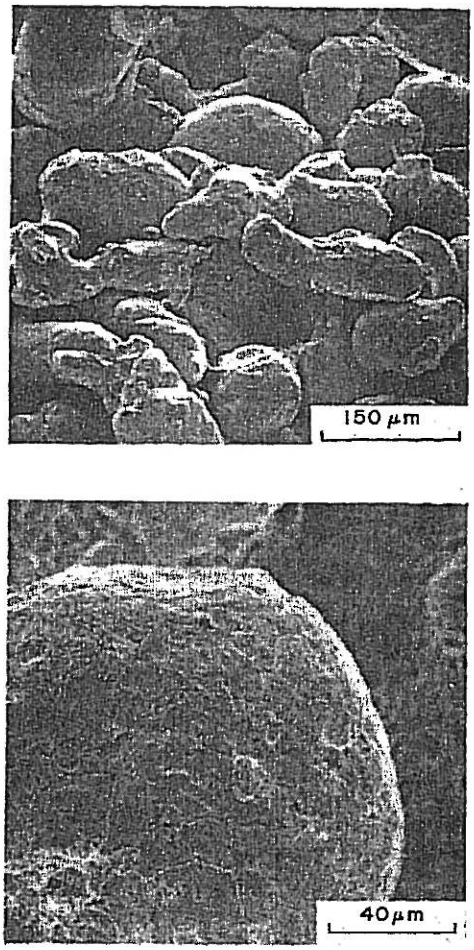

Fig. 2. Scanning micrographs of the lead powder showing (a) the irregular shape and (b) a lead particle after cleaning: the grain boundaries are now visible.

2.3. *Density measurements*

Density–time curves, at constant pressure and temperature, are obtained from the output of the strain gauges via a calibration curve [15]. A typical density–time plot is shown in Fig. 5. It is convenient, for later manipulation, to fit the data to an empirical relation [16]

$$\frac{\frac{\Delta}{\Delta_0}-C_1}{C_2-\frac{\Delta}{\Delta_0}}=kt^m. \tag{2}$$

The constants C_1, C_2, k and m are determined using a linear regression analysis [13]. The fit shown in Fig. 5 is typical. Densification-rates are obtained by differentiating equation (2) giving

$$\frac{\Delta}{\Delta_0}=\frac{mk\left(C_2-\frac{\Delta}{\Delta_0}\right)^{m-1}}{1+kt^m}. \tag{3}$$

A typical plot of densification-rate vs density is shown in Fig. 6. Equations (2) and (3) are used only for curve-fitting to get densification-rates, and have no fundamental significance. The final relative density, Δ_f/Δ_0, of each specimen is measured by an immersion

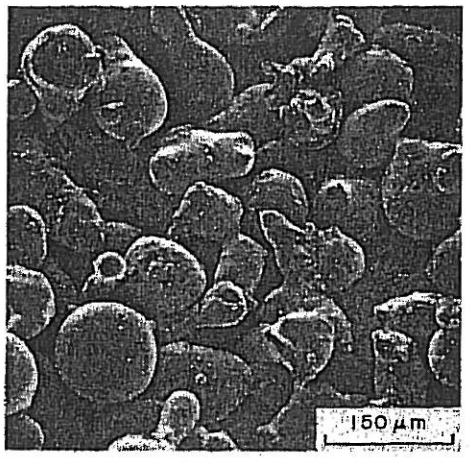

Fig. 3. A scanning micrograph of the tin powder.

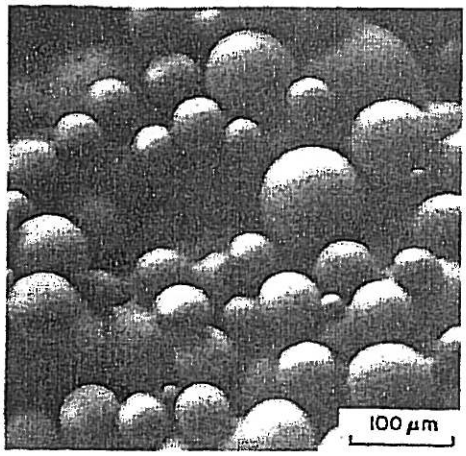

Fig. 4. A scanning micrograph of the PMMA powder.

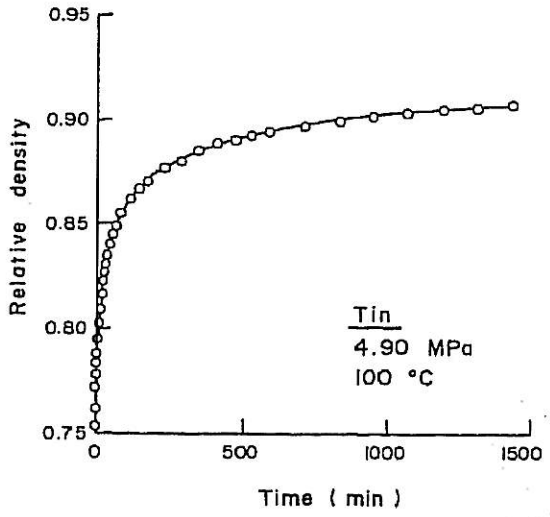

Fig. 5. A typical density–time plot from the experimental data (circles). The full line is the empirical equation (2) fitted to the data.

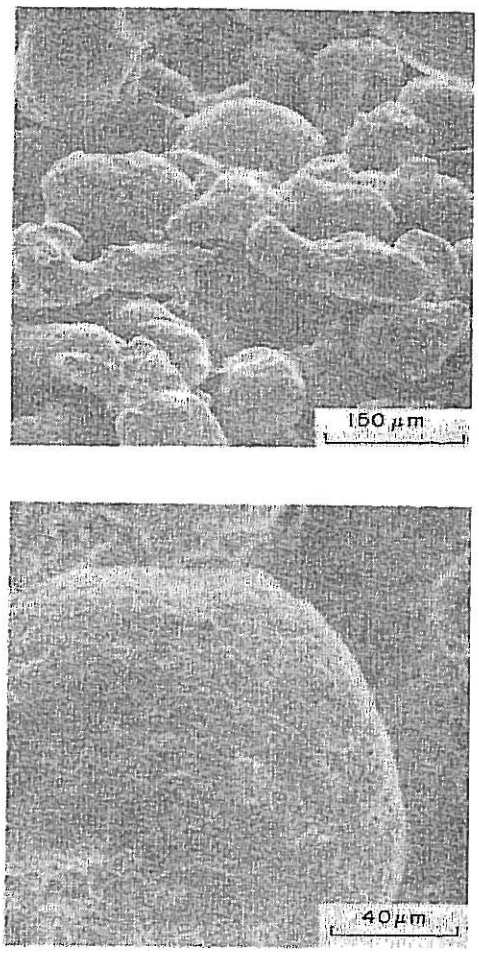

Fig. 2. Scanning micrographs of the lead powder showing (a) the irregular shape and (b) a lead particle after cleaning: the grain boundaries are now visible.

2.3. *Density measurements*

Density–time curves, at constant pressure and temperature, are obtained from the output of the strain gauges via a calibration curve [15]. A typical density–time plot is shown in Fig. 5. It is convenient, for later manipulation, to fit the data to an empirical relation [16]

$$\frac{\dfrac{\Delta}{\Delta_0} - C_1}{C_2 - \dfrac{\Delta}{\Delta_0}} = kt^m. \tag{2}$$

The constants C_1, C_2, k and m are determined using a linear regression analysis [13]. The fit shown in Fig. 5 is typical. Densification-rates are obtained by differentiating equation (2) giving

$$\frac{\Delta}{\Delta_0} = \frac{mk\left(C_2 - \dfrac{\Delta}{\Delta_0}\right)^{1m-1}}{1 + kt^m}. \tag{3}$$

A typical plot of densification-rate vs density is shown in Fig. 6. Equations (2) and (3) are used only for curve-fitting to get densification-rates, and have no fundamental significance. The final relative density, Δ_f/Δ_0, of each specimen is measured by an immersion

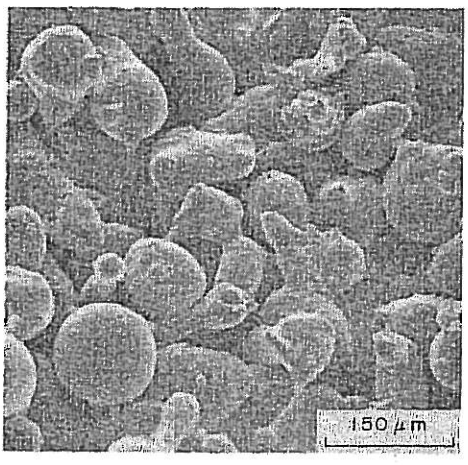

Fig. 3. A scanning micrograph of the tin powder.

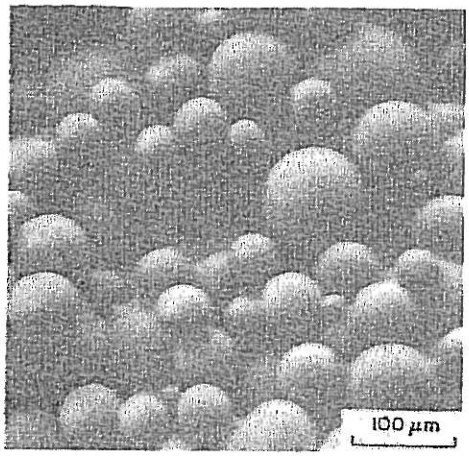

Fig. 4. A scanning micrograph of the PMMA powder.

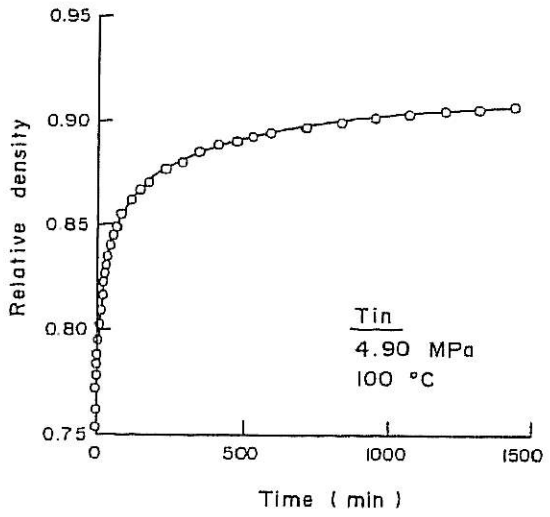

Fig. 5. A typical density–time plot from the experimental data (circles). The full line is the empirical equation (2) fitted to the data.

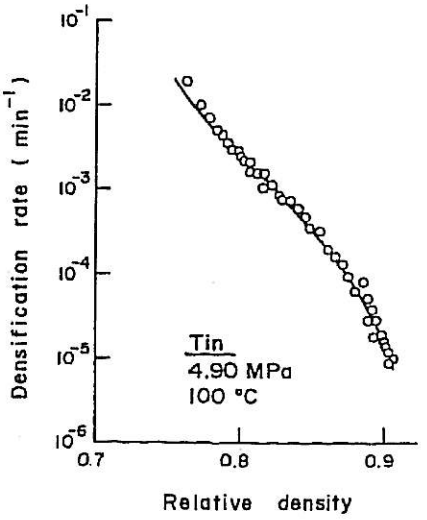

Fig. 6. A typical densification-rate vs density plot. The circles show the slope of the line joining adjacent points on Fig. 5; the full line is eqation (3).

Table 2. Initial and final relative densities for pressure sintering of tin

Pressure (MPa)	Temperature, (°C) 27	51	75	100	125	150
1.38						0.644
						0.820
2.07					0.670	0.695
					0.868	0.876
3.10				0.691	0.676	0.741
				0.851	0.916	0.925
4.90			0.708	0.722	0.745	0.780
			0.864	0.907	0.932	0.959
6.97		0.734	0.730	0.774	0.842	
		0.864	0.903	0.939	0.964	
10.48	0.756	0.789	0.796	0.823		
	0.871	0.919	0.944	0.967		
13.79	0.793	0.823	0.864			
	0.915	0.949	0.966			

Notes: 1. Top figure is the zero-time relative density and the bottom figure is the final relative density.
2. All tests were for 24 h.
3. Average particle diameter = 150 μm.

method [17] at the end of each test, for calibration purposes.

2.4. Creep tests

Compacts of lead and tin with less than 1% porosity were prepared by pressure sintering for 30 min, at 150°C and 60 MPa. Cylindrical creep-specimens were machined from these compacts. Others were made by chill-casting, using the lead and tin powders as source material. Compressive creep tests were carried out on both sets of specimens to determine the creep constants for the solid material.

3. EXPERIMENTAL RESULTS

3.1. Densification data

The initial and final densities for tests on lead and tin, at each pressure and temperature, are listed in Tables 1 and 2. Figures 7 and 8 show density as a function of time at 100°C for the two metals. Densification-rates were calculated by the procedure outlined above, to give the results shown in Figs 9 and 10. The power-law relating densification-rate to pressure is obtained by cross-plotting the data as shown in Figs 11 and 12. An exponent of 6.5 was found for both lead and tin at 100°C, agreeing well with that for steady-state creep of cast samples of the same materials (see below).

3.2. Pore geometry

Figure 13 shows a density–time plot for PMMA powder, sintered at 110°C and 0.7 MPa. The scanning electron micrographs show that circular contact necks form at short times, with no pore rounding. As the necks grow, the free surfaces of the particles move into the pore space maintaining a sharply cusped pore shape, and the number of contact-neighbours per particle

Table 1. Initial and final relative densities for pressure sintering of lead

Pressure (MPa)	Temperature, (°C) 27	51	75	100	125	150
3.52						0.698
						0.877
4.90					0.749	0.758
					0.901	0.916
6.21				0.761	0.758	0.779
				0.908	0.920	0.938
7.59			0.782	0.789	0.814	0.830
			0.914	0.922	0.938	0.947
8.97		0.786	0.784	0.808	0.856	0.855
		0.921	0.916	0.935	0.949	0.959
10.35	0.787	0.809	0.831	0.841	0.857	
	0.898	0.913	0.939	0.946	0.961	

Notes: 1. Top figure is the zero-time relative density and the bottom figure is the final relative density.
2. All tests were for 24 h.
3. Average particle diameter = 150 μm.

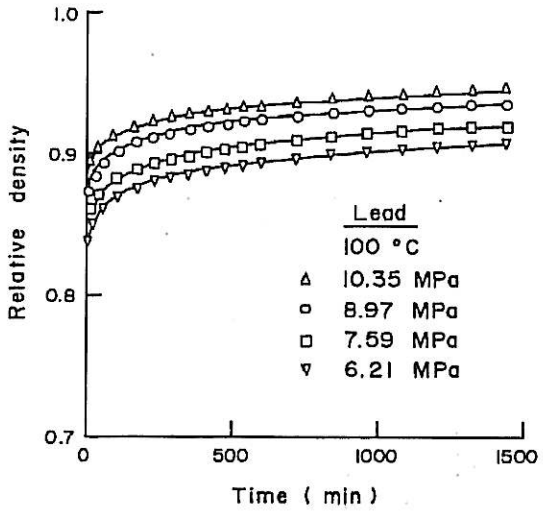

Fig. 7. The density–time data for pressure sintering of lead at 100°C.

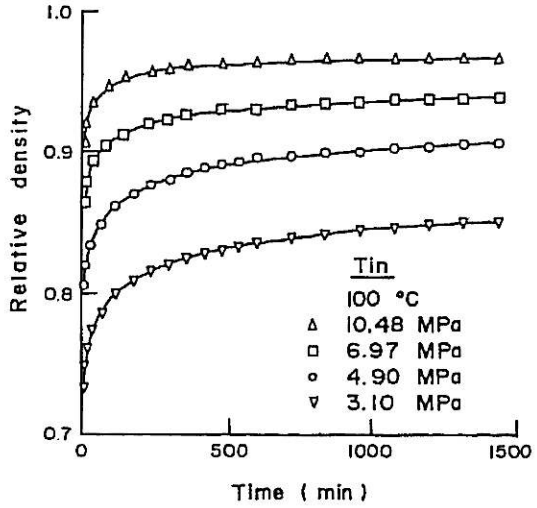

Fig. 8. The density–time data for pressure sintering of tin at 100°C.

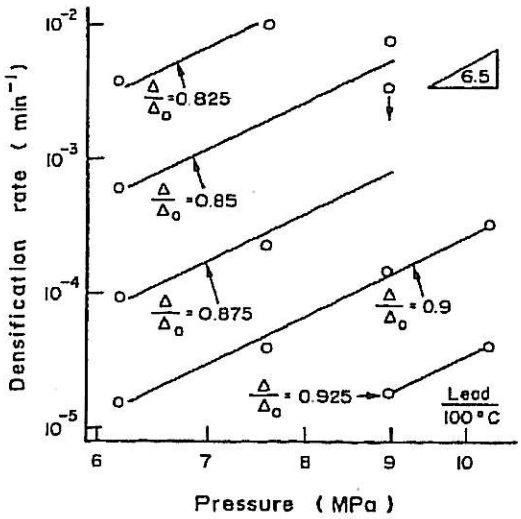

Fig. 11. The pressure dependence of the densification-rate at constant density for lead at 100°C.

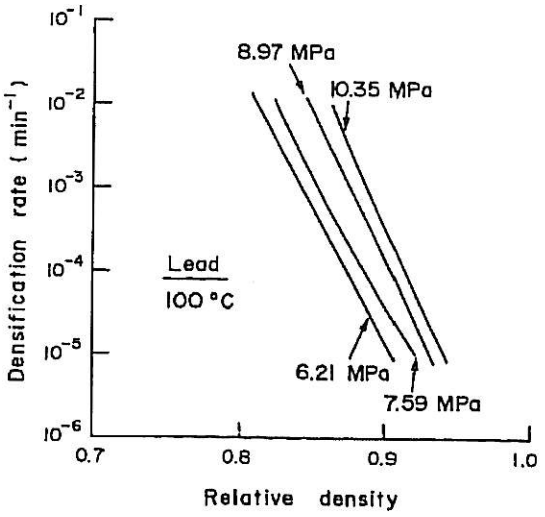

Fig. 9. The densification-rate vs density for lead at 100°C.

increases. Pore rounding occurs only at high densities when growing necks impinge on each other, and the rate of neck growth is low. Optical micrographs of lead and tin compacts (Figs 14 and 15) show the same thing. This pore geometry is quite different from that which develops during pressureless sintering and which is used in models for pressure sintering. We thus need to modify the models, as discussed below.

3.3. *Uniaxial compressive creep tests*

Creep data at constant load for sintered and chill-cast specimens of lead and tin are shown in Figs 16 and 17. In both cases, the sintered material is more creep-resistant than the chill-cast material because (we believe) of the oxide coating on the particles. The data from case samples are in good agreement with other published results.

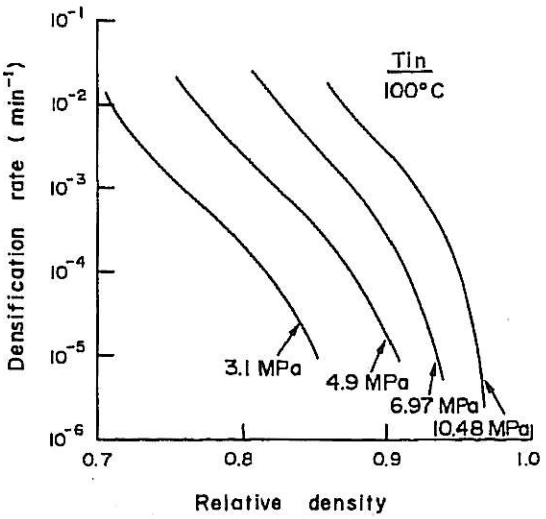

Fig. 10. The densification-rate vs density for tin at 100°C.

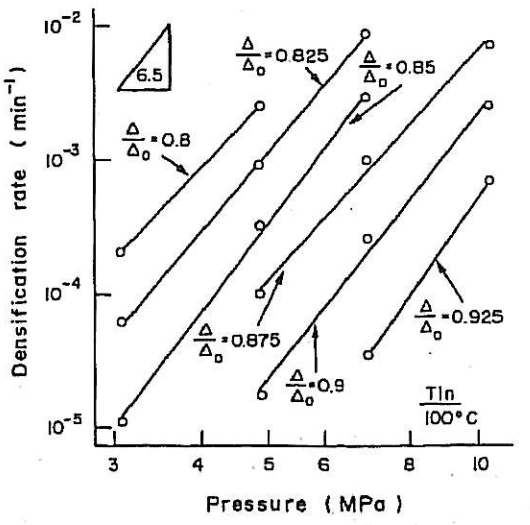

Fig. 12. The pressure dependence of the densification-rate at constant density for tin at 100°C.

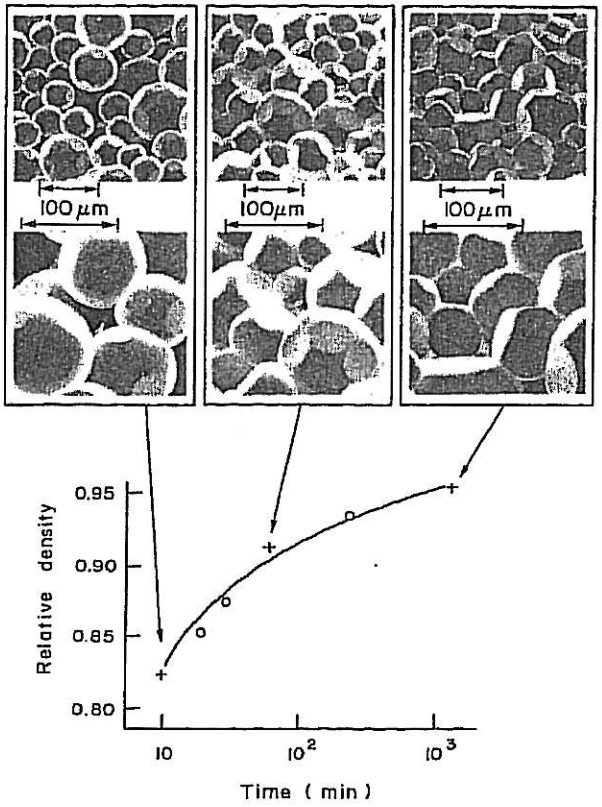

Fig. 13. Density–time plot for sintering of PMMA at 110°C and 0.7 MPa. Even at high densities the pores are cusped instead of rounded.

4. MODELS FOR PRESSURE SINTERING

In this section we review existing models for sintering under pressure: plastic yielding, viscous flow, and power-law creep. Diffusional processes also contribute to sintering, and these, too, are accelerated by pressure, which adds to the surface-tension driving force. But since they do not contribute significantly in the experiments discussed here we shall not discuss them further.

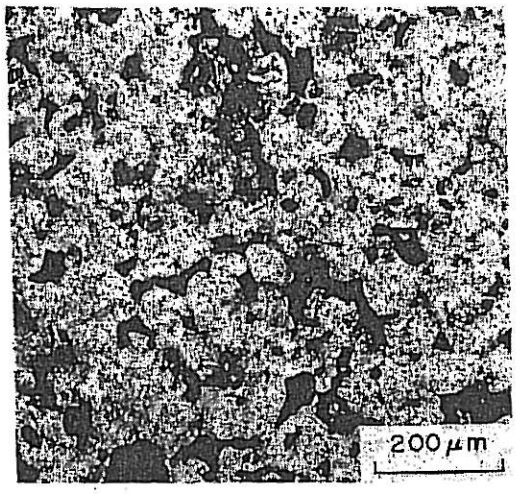

Fig. 14. Pore structure of lead after pressure sintering for 24 h at 150°C and 2.52 MPa (87.7% density). Note the cusped pore shapes.

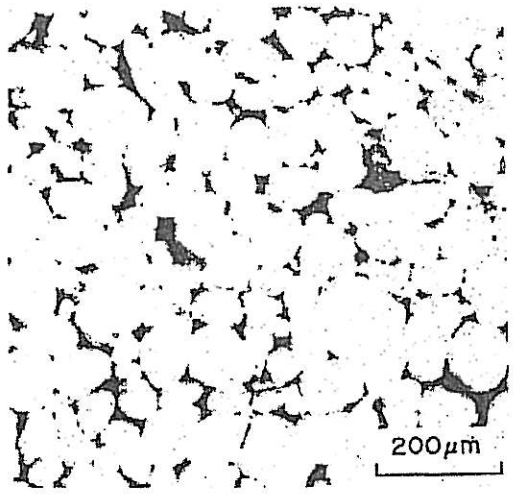

Fig. 15. Pore structure of tin after pressure sintering for 24 h at 150°C and 2.07 MPa (87.6% density). Note the cusped pore shape.

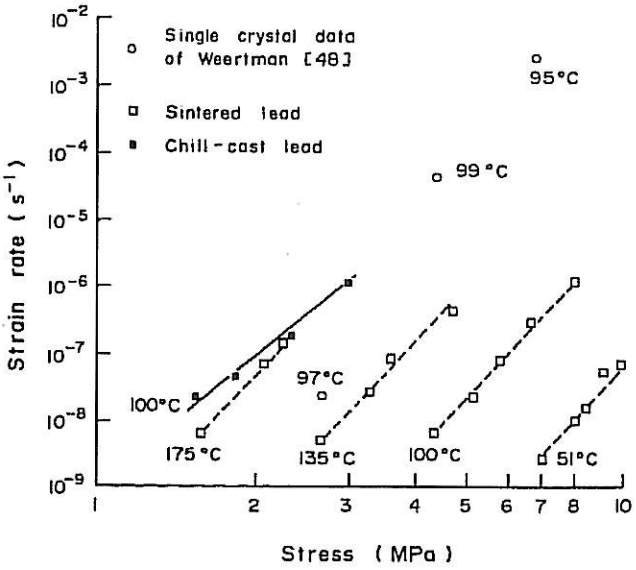

Fig. 16. Steady-state creep data for lead.

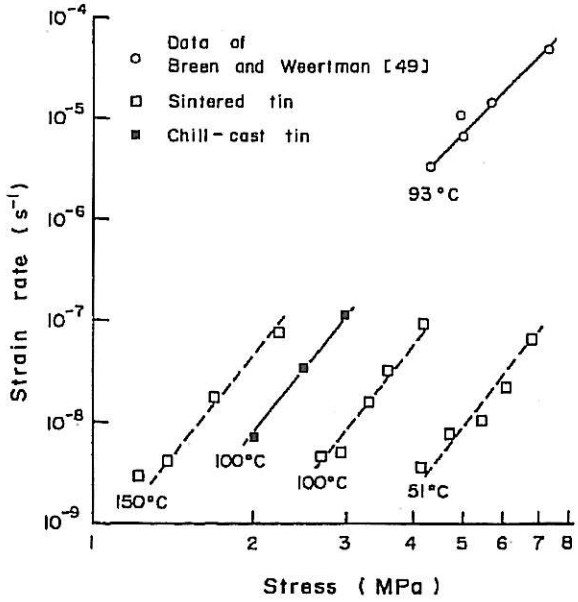

Fig. 17. Steady-state creep data for tin.

It is usual in modelling sintering to distinguish two stages, according to the geometry of the pores. During the *initial stage* the compact is idealised as an aggregate of individual particles with small, sharply curved contacts between them. During the *final stage*, the pores are idealised as an array of isolated spherical holes. Some authors introduce a further *intermediate stage*, idealising the pores as a connected network of cyclindrical holes, but the approximation is a poor one, and is seldom useful [13] except for interpolating between the initial and final stages. The models described below refer to these stages.

4.1. Plastic yielding

If the external applied pressure p_e is large enough, the flow strength of the material is exceeded locally where particles touch. Approximate solutions exist for the contact area which results when spheres of a perfectly plastic solid are passed together (Fig. 18). For initial-stage densification, models based on the slip-line field solution for a flat punch indenting an infinite plastic half-space [18] have been developed [5, 6]. The neck grows until the local indentation pressure, p_1, is

$$p_1 \approx 3\sigma_y \tag{4}$$

where σ_y is the tensile flow strength of the material of the particle. If the co-ordination number remains constant, simple geometry [5, 6] relates the density Δ to the initial density Δ_i and neck radius x

$$\frac{\Delta}{\Delta_0} = \frac{\Delta_i}{\Delta_0}\left[1+\frac{3}{2}\left(\frac{x}{a}\right)^2\right] \tag{5}$$

where a is the particle radius. The equilibrium condition [equation (4)] then gives the density as a function of external pressure

$$\frac{\Delta}{\Delta_0} = \frac{\Delta_i}{\Delta_0}\left(1+\frac{p_e A_f}{2\pi n_f \sigma_y a^2}\right) \tag{6}$$

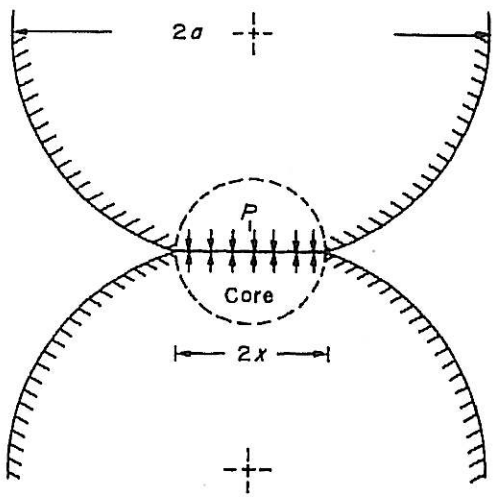

Fig. 18. The stage 1 model for pressure sintering. Each sphere indents the other.

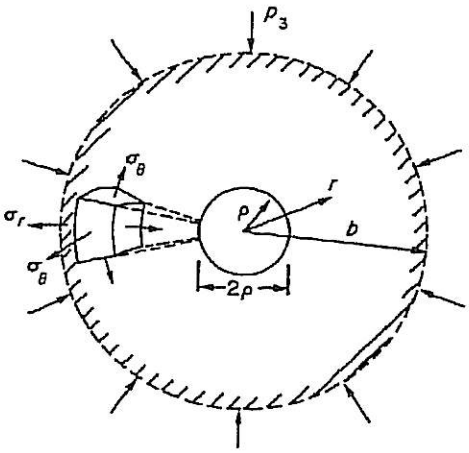

Fig. 19. The stage 3 model for pressure sintering based on the creep of a thick spherical shell of inner radius ρ and outer radius b.

where A_f is the surface area of a cell containing one particle (roughly $4\pi a^2$) and n_f is the number of contacts (co-ordination number) of a particle.

Final stage densification is modelled as the plastic collapse of a thick spherical shell with the pore at its centre [4], as shown in Fig. 19. Yielding occurs if

$$p_3 > -\tfrac{2}{3}\sigma_y \ln\left(1-\frac{\Delta}{\Delta_0}\right). \tag{7}$$

Here p_3 is the driving pressure for densification during this stage given by

$$p_3 = p_e - p_i + 2\gamma_s/\rho$$

where p_i is the internal gas pressure in the pore, ρ is the pore radius and γ_s its surface energy.

The intermediate stage is modelled by replacing the spherical shell by a cylindrical one, constrained by the compact along the axis of the porosity [14]. Yielding then occurs until

$$p_2 > -\frac{\sigma_y}{\sqrt{3}} \ln\left(1-\frac{\Delta}{\Delta_0}\right) \tag{8}$$

where $p_2 = p_e + \gamma_s/\rho$. (Since porosity is open during this stage, $p_i = 0$.)

In addition to these model-based equations, certain empirical relationships have been proposed which relate the density of a compact to the pressure. That of Heckel [19, 20] likens compaction to a first-order chemical reaction

$$\frac{\mathrm{d}(\Delta/\Delta_0)}{\mathrm{d}(p_e/\sigma_y)} = K\left(1-\frac{\Delta}{\Delta_0}\right) \tag{9}$$

which, upon integration, gives

$$\ln\left(\frac{1}{1-\Delta/\Delta_0}\right) = K_1\frac{0_e}{\sigma_y} + K_2 \tag{10}$$

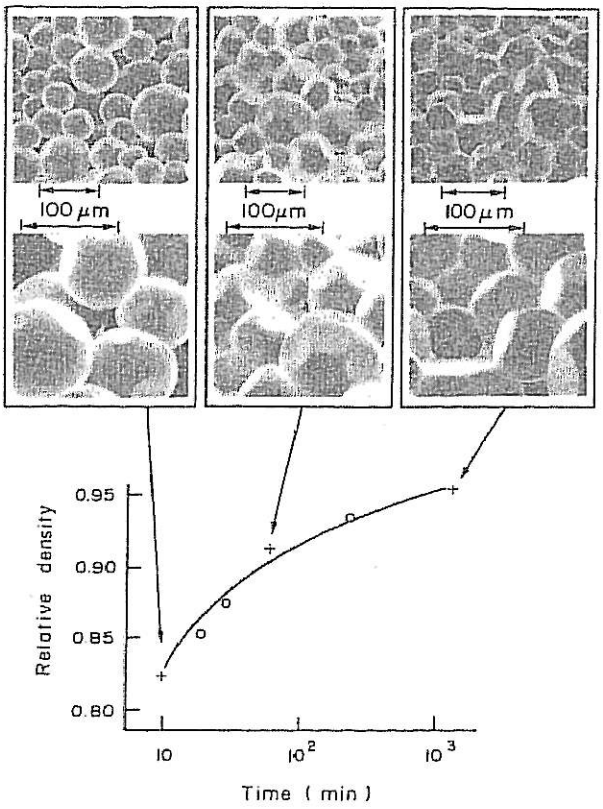

Fig. 13. Density–time plot for sintering of PMMA at 110°C and 0.7 MPa. Even at high densities the pores are cusped instead of rounded.

4. MODELS FOR PRESSURE SINTERING

In this section we review existing models for sintering under pressure: plastic yielding, viscous flow, and power-law creep. Diffusional processes also contribute to sintering, and these, too, are accelerated by pressure, which adds to the surface-tension driving force. But since they do not contribute significantly in the experiments discussed here we shall not discuss them further.

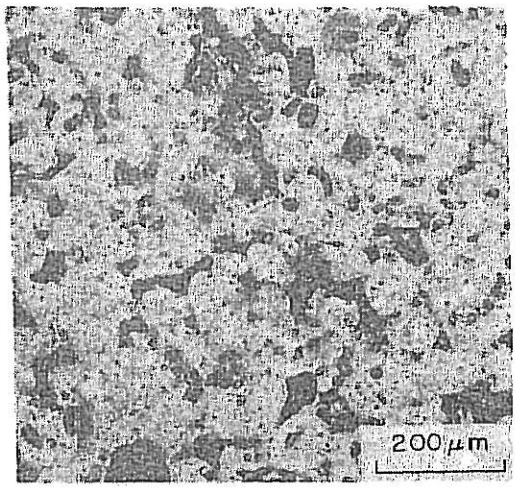

Fig. 14. Pore structure of lead after pressure sintering for 24 h at 150°C and 2.52 MPa (87.7% density). Note the cusped pore shapes.

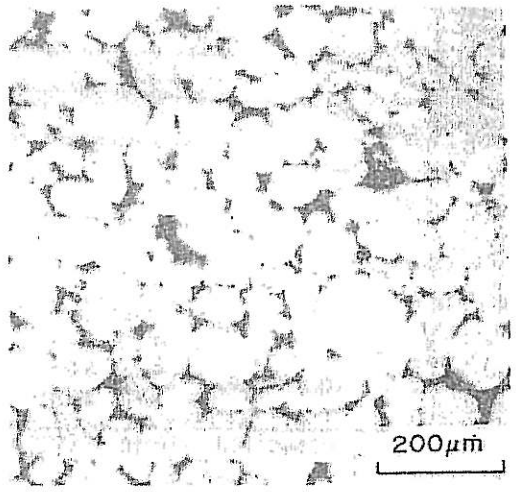

Fig. 15. Pore structure of tin after pressure sintering for 24 h at 150°C and 2.07 MPa (87.6% density). Note the cusped pore shape.

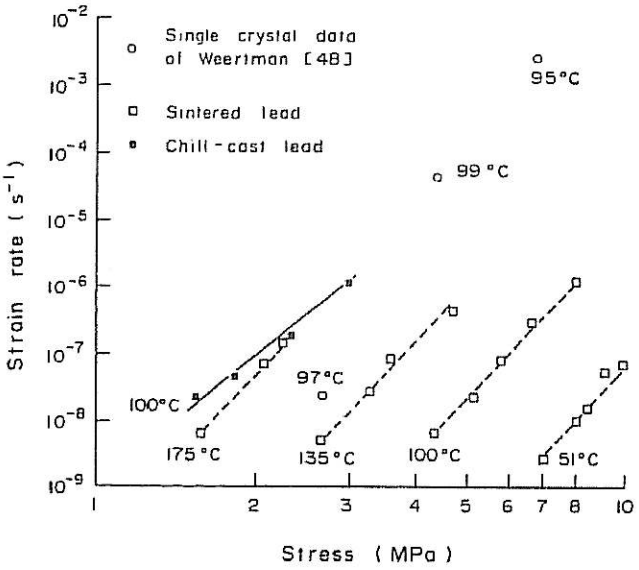

Fig. 16. Steady-state creep data for lead.

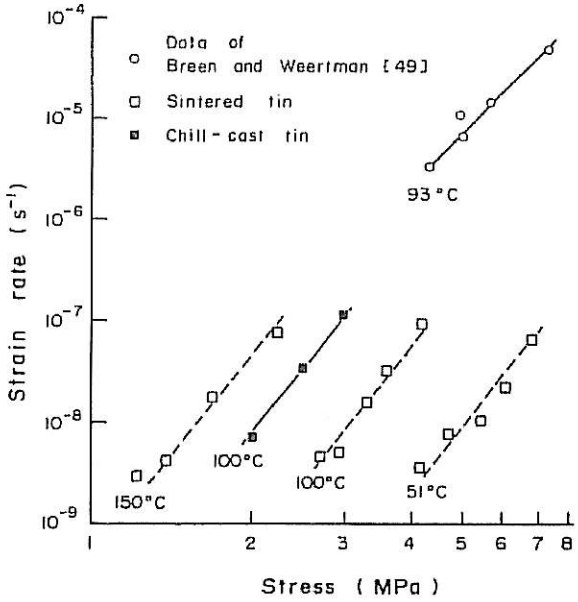

Fig. 17. Steady-state creep data for tin.

where K_1 and K_2 are dimensionless constants. Note that if K_1 is set equal to $\frac{3}{2}$, equation (10) is almost identical with equation (7). Moreover, at low Δ/Δ_0 it reduces to an equation with the form of equation (5). Thus it approximates both the initial and final stage models. It has been found to fit the compaction data of iron, copper, nickel and tungsten powder well over a wide range of pressures and densities. This fit means that the models, too, are a good description.

4.2. *Viscous flow*

The earliest theories of pressure sintering were based on Newtonian-viscous flow, as in a liquid. Murray *et al.* [21] adapted a theory for final stage pressureless sintering of MacKenzie and Shuttleworth [22] by replacing the capillary pressure $2\gamma_s/\rho$ by the applied pressure p_e, giving

$$\frac{\dot{\Delta}}{\Delta_0} = \frac{3p_e}{4\eta}\left(1-\frac{\Delta}{\Delta_o}\right) \tag{11}$$

where η is the viscosity. Integration with respect to time t gives

$$\ln\left(\frac{1-\Delta/\Delta_0}{1-\Delta_i/\Delta_0}\right) = -\frac{3p_e^t}{4\eta}. \tag{12}$$

The model works well for Newtonian viscous materials such as fused silica [23], but it does not adequately describe the hot-pressing either of metals [24] or of ceramics [25, 26].

4.3. *Power-law creep*

When Williams [24] tried to fit equation (11) to hot-pressing data for copper, iron, aluminium, thorium, zirconium, silver, magnesium and beryllium, he did not find a linear relationship between densification rate, $\dot{\Delta}/\Delta_0$, and applied pressure, p_e; instead, he observed a power-law

$$\frac{\dot{\Delta}}{\Delta_0} \propto p_e^n \tag{13}$$

with a power, n, greater than 1. Similar behaviour was observed for lead [27], and in our own experiments (Section 3). This suggests a new mechanism, one involving power-law creep [8, 9, 28–31].

The most complete treatment is that of Wilkinson and Ashby [8] who developed models for each of the stages of pressure sintering using a constitutive law for power-law creep of the form

$$\dot{\varepsilon}_{ss} = A\sigma^n \tag{14}$$

where A is a temperature-dependent constant. Final stage densification is modelled by using the creep of a thick-walled spherical shell centred on a pore (Fig. 19). The outer radius of the shell, b, is defined, such that matter is conserved

$$\frac{\Delta}{\Delta_0} = 1-\left(\frac{\rho}{b}\right)^3 \tag{15}$$

where ρ is the pore radius. The densification-rate is given by

$$\frac{\dot{\Delta}}{\Delta_0} = \frac{A\dfrac{\Delta}{\Delta_0}\left(1-\dfrac{\Delta}{\Delta_0}\right)}{2\left[1-\left(1-\dfrac{\Delta}{\Delta_0}\right)^{1/n}\right]^n}\left(\frac{3}{2n}p_3\right)^n. \tag{16}$$

Densification during the intermediate stage is modelled by replacing the spherical shell by a cylindrical one giving [8]

$$\frac{\dot{\Delta}}{\Delta_0} = \frac{\sqrt{3}\,A\dfrac{\Delta}{\Delta_0}\left(1-\dfrac{\Delta}{\Delta_0}\right)}{\left[1-\left(1-\dfrac{\Delta}{\Delta_0}\right)^{1/n}\right]^n}\left(\frac{\sqrt{3}}{n}p_2\right)^n. \tag{17}$$

For the initial stage, Wilkinson and Ashby [8] develop a model by drawing on theories for hot hardness tests [32, 33]. Here it is assumed that a hemispherical "core" with radius x, attached to the contact face, remains rigid during indentation. Since this core expands into the surrounding material, the stresses and deformations are the same as those due to pressure in a spherical cavity (Fig. 18). The problem reduces to that of a spherical shell containing an internal pressure, and a solution follows in the same way as that for final stage sintering. The result is

$$\frac{\dot{\Delta}}{\Delta_0} = \frac{3}{4\pi}\left(\frac{\Delta}{\Delta_0}\right)^2\frac{n_f A_f x}{a^3}A\left(\frac{3}{2n}\frac{A_f}{\pi x^2}p_e\right)^n \tag{18}$$

where n_f is the co-ordination number of the particle, and A_f is the surface area of the "cell" containing one particle [5, 6, 14].

This model contains some questionable assumptions. First, the number of contacts per particle n_f, is assumed constant; in reality it increases with density. Second, the pore is assumed to be rounded; our observations and those of Matthews [34] show that it remains cuspy. The average pressure on the contacts, p_1, is greatly influenced by these aspects of the geometry, as is the relationship between neck size and density. Improvements to the model are discussed in Section 6, below.

5. ANALYSIS OF DATA, AND COMPARISON WITH MODELS

The conditions of our experiments were chosen so that, almost always, plastic yielding and power-law creep were the dominant mechanisms of densification. In this section we compare our measurements with the appropriate model from Section 4, using material data given in Table 3. We find that agreement is poor.

5.1. *Plastic yielding*

In our experiments it took 30 s to fully apply the pressure. We assume that densification during that time is by plastic yielding only, and compare the density after 30 s with the models for plastic yielding. To do this, we first plot the data in terms of the empirical relationship

Table 3. Material data

Property	Lead		Tin	
Atomic volume, (m^3)	3.03×10^{-29}		2.76×10^{-29}	
Burgers' vector, b (m)	3.49×10^{-10}		3.02×10^{-10}	
Melting point, T_m(K)	600		505	
Density, Δ_0(kg/m^3)	1.14×10^4		7.3×10^3	
Shear modulus, μ (MN/m^2)	7.4×10^3	[38]	1.56×10^4	[29]
T-coefficient of μ (K^{-1})	-1.28×10^{-3}	[38]	-2.75×10^{-3}	[39]
Surface energy, γ_s(J/m)	0.61	[40]	0.68	[41]
Pre-exp. lattice diff., D_{0v}(m^2/s)	1.37×10^{-4}	[40]	9.1×10^{-4}	[43]
Activ. energy, lattice diff., Q_v(kJ/mol)	109	[42]	105	[43]
Pre-exp. boundary diff., $\delta_b D_{0b}$(m^3/s)	8.1×10^{-14}	[44]	3.0×10^{-15}	[45]
Activ. energy, boundary diff., Q_b(kJ/mol)	65.7	[44]	39.9	[45]
Pre-exp. surface diff., $\delta_s D_{0b}$(m^3/s)	2.6×10^{-11}	[46]	2.2×10^{-11}	[46]
Activ. energy, surface diff., Q_s(kJ/mol)	75	[46]	64	[46]
Pre-exp. vapourisation, P_0(MN/m^2)	7.9×10^3	[47]	1.0×10^4	[47]
Activ. energy, vapourisation, Q_{vap}(kJ/mol)	186	[47]	285	[47]
Power-lax creep constant, A'(m^2/s)	2.5×10^8	[48]	5.5×10^{14}	[49]
Power-law creep exponent, n	5	[48]	6.6	[49]
Activ. energy, power-law creep Q_{crp}kJ/mol)	96	[48]	94	[49]
Yield stress, σ_y(MN/m^2)	18.5	[50]	21.8	[50]
T-dependence of yield, C_T(K^{-1})	4.8×10^{-3}	[51]	3.7×10^{-3}	[52]

†Approximated by $\delta_s D_{0s} \approx 0.074\, b$ m^3/s and $Q_s \approx 0.125\, T_M$kJ/mol.

[19, 20] given by equation (10) (which provides a convenient framework in which experiment and theory can be compared). The temperature dependence of the yield stress can be approximated by

$$\sigma_y = \sigma_{y0}[1-(T-300)C_T] \qquad (19)$$

where σ_{y0} is the yield stress at 300 K, T is the absolute temperature, and C_T is a temperature coefficient. Combining equations (10) and (19) gives

$$\ln \frac{1}{1-\frac{\Delta}{\Delta_0}} = \frac{K_1 p_e}{\sigma_{y0}[1-(T-300)C_T]} + K_2. \qquad (20)$$

Using published values for the 300 K yield stress (Table 3) K_1, K_2 and C_T are found by a linear regression analysis. Figures 20 and 21 show the densities of lead and tin after 30 s on a plot of $\ln [1/(1-\Delta/\Delta_0)]$ vs the normalised pressure, p_e/σ_y. The models for plastic yielding described in Section 4 are plotted on Figs 20 and 21 as broken lines. Agreement is poor.

5.2. *Power-law creep*

Figures 22 and 23 show the data for the subsequent densification-rate at constant pressure, for tin and lead, compared with the power-law creep models described in Section 4. Figure 22 is for lead sintered at 150°C and 3.5 MPa, and Fig. 23 is for tin sintered at 150°C and 3.1 MPa. Under these conditions, power-law creep is the dominant mechanism. The experimental densification-rates are about two orders of magnitude slower than the models predict.

6. MODIFICATIONS TO PRESSURE SINTERING MODELS

In this section, we re-examine the sintering models, and modify them in a physically sensible way. The modified models give better agreement with experiment.

6.1. *Neck geometry and co-ordination number*

When spherical particles are sintered, the neck shape depends on the relative contributions of the mechanisms involved: diffusion gives pore-rounding, while plastic flow and power-law creep give cusped pores. When both diffusion and creep contribute, the shape lies somewhere in between these extremes. The shape is important because the maximum curvature at the neck determines the driving force for the non-densifying mechanisms (such as surface diffusion), and influences that for certain densifying mechanisms (such as boundary diffusion). It also affects the contact area between particles, and thus the contact pressure at the neck.

When plastic yielding and power-law creep are the dominant mechanisms, our observations suggest that the geometry of the neck is as shown in Fig. 24. Material enters the neck in such a way that the free surface of the particle expands outwards into the pore, remaining a

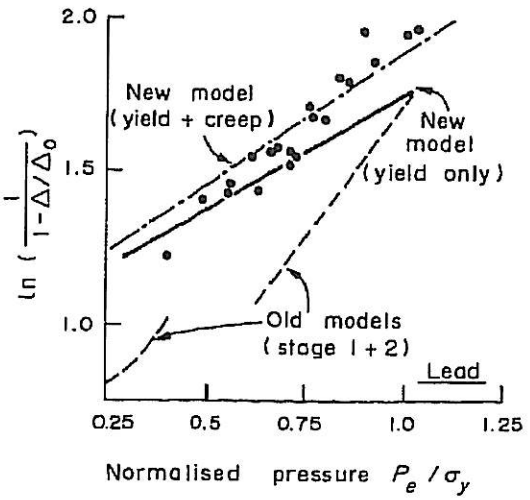

Fig. 20. Densification data for lead by plastic yielding (30 s density). Previous models [equations (6), (7) and (8)] are shown as broken lines. The full line shows the modified model [equation (23)]. The dash-dot line shows the modified model plus power-law creep for 20 s.

segment of a sphere as it does so. The effective particle radius increases as densification advances, and the pore remains cuspy. Once full density is reached, the initially spherical particles have become polyhedra.

A second important aspect is the geometry of the particle packing. During densification, the average number of contacts per particle (the co-ordination number n_f) increases steadily [3]. At the same time existing contacts grow in area (Fig. 24). Both processes cause the effective pressure on a particle contact to decrease during densification. Yielding and power-law creep are highly stress-sensitive, so these geometrical changes are strongly reflected in the densification-rates of the powder.

6.2. *Plastic yielding*

It has been shown recently [35, 36] that, starting from a dense random packing of spherical particles, the evolution of the contact area (πx^2) and the co-ordination number (n_f) can be calculated. The results agree well with model experiments [35, 36]. For cusp-like neck geometry of Fig. 24, the contact area is given by

$$A_c = \pi x^2 = 3\,\frac{(\Delta-\Delta_i)}{\Delta_0}\,a^2 \qquad (21)$$

and the co-ordination number by

$$n_f = n_{f,i} + 9.5\,\frac{\Delta-\Delta_i}{\Delta_0} \quad \text{for} \quad \frac{\Delta}{\Delta_0} < 0.85$$

$$= n_{f,i} + 2 + 9.5\left(\frac{\Delta}{\Delta_0} - 0.85\right) + 881\left(\frac{\Delta}{\Delta_0} - 0.85\right)^3 \quad \text{for} \quad \frac{\Delta}{\Delta_0} \geq 0.85 \qquad (22)$$

where $\Delta_i/\Delta_0 = 0.64$ and $n_{f,i} = 7.3$ are the initial density and initial average co-ordination number of the dense random packing of spheres. Using equation (21), the effective pressure acting on a particle contact can be expressed as a function of the relative density, and the external pressure p_e

$$p_{\text{eff}} = \frac{4\,a^2\,\Delta_0}{x^2\,n_f\Delta}\,p_e. \qquad (23)$$

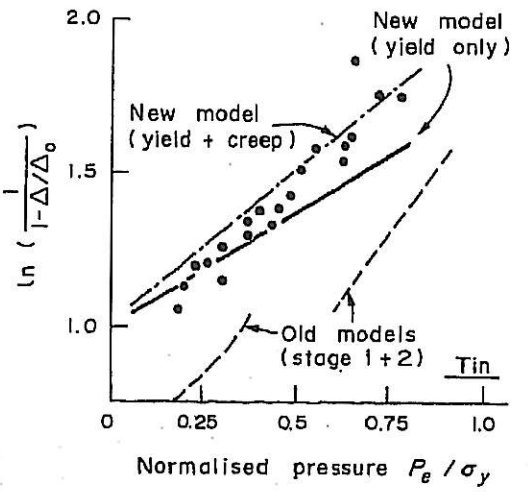

Fig. 21. A similar plot to Fig. 20 for the densification data tin by plastic yielding (30 s density).

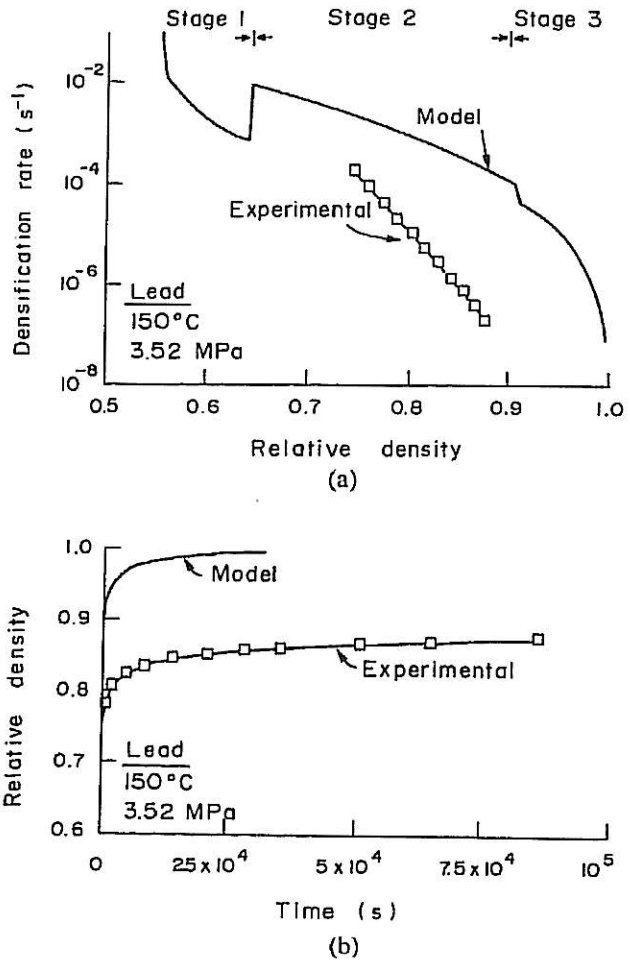

Fig. 22. Densification data for lead when power-law creep is dominant, compared with the models of Section 4. (a) Densification-rate; (b) density.

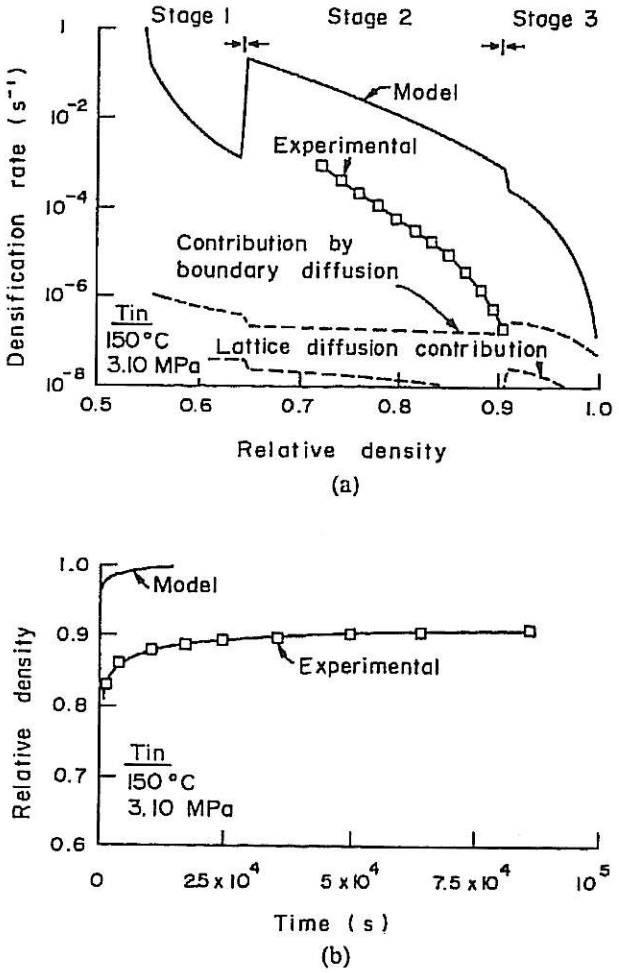

Fig. 23. Densification data for tin when power-law creep is dominant, compared with the models of Section 4. (a) Densification-rate; (b) density.

Plastic yielding occurs as long as $p_{eff} \geq 3\sigma_y$ [equation (4)]. This result is plotted as solid lines in Figs 20 and 21. The agreement is much better than for previous models, although, at high pressures, the densities are systematically underestimated.

There is an explanation for this discrepancy. It takes about 30 s to reach the test pressure; it is thus 30 s density which is plotted in the figures. The initial pressurisation is rapid, so that most of this time is spent near the final pressure. Some of the initial densification, particularly at high pressures, may be due to an additional contribution of power-law creep. This is supported by the dash-dot curves in Figs 20 and 21, which include (using the method outlined in the following section) the additional densification by power-law creep, assuming the full test pressure to be maintained for 20 s out of the total of 30 s.

6.3. *Power-law creep*

The particle-indentation model for initial-stage sintering which incorporates the increase in co-ordination, can be extended to power-law creep. An exact solution for the constrained creep indentation at the contact faces is difficult, but a dimensional argument [37] leads to the following approximate solution

$$\frac{\dot{\Delta}}{\Delta_0} = 5.3 \left(\frac{\Delta}{\Delta_0}\right)^{2/3} \left(\frac{\Delta_i}{\Delta_0}\right)^{1/3} \frac{x}{a} A \left(\frac{p_{eff}}{3}\right)^n. \quad (24)$$

It differs from equation [18] both in the treatment of the indentation process [37] and in allowing the co-ordination number to increase with density. The factor $\frac{1}{3}$ in the brackets is again a "constraint" factor [as in equation (4)] which reflects the indentation-like geometry; and p_{eff} is given by equation [23].

A comparison of this equation with experiment is shown in Fig. 25. For this purpose the creep data (A and n) of the chill-cast materials (Figs 16 and 17) are used. The figure also shows the prediction of equation (16) for final stage sintering by power-law creep. The two curves together predict the densification behaviour of both lead and tin moderately well. A "switch-over" from first stage to final stage behaviour occurs at a density of about $\Delta/\Delta_0 \sim 0.95$.

7. CONCLUSIONS

The application of a pressure during sintering enhances some of the mechanisms of pressureless sintering and introduces others which are new. We have investigated two of the new mechanisms: plastic yielding and power-law creep. To do so, we have studied the densification of lead, tin and PMMA powders in a specially-constructed hydrostatic press.

Published models for the densification of a powder compact by these two mechanisms do not agree with the data. The models are deficient in at least two regards: they assume a constant co-ordination number for a particle, whereas in reality, it increases with density; and they assume a rounded pore shape, whereas in reality it is sharply cusped. We have modified the models to include both these effects. In

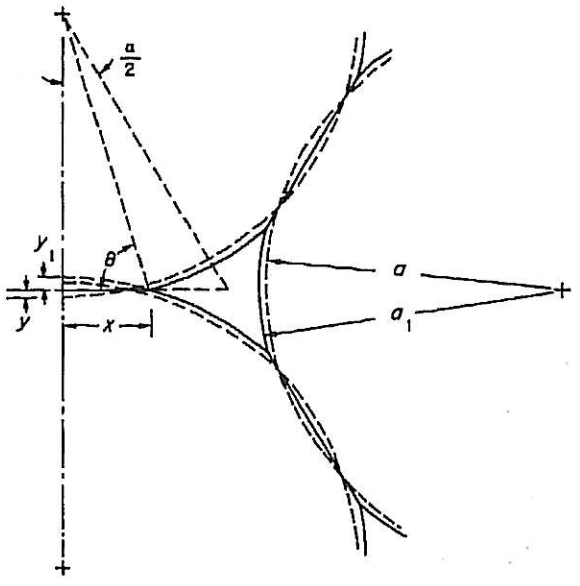

Fig. 24. A section through 3 particles during plastic yielding and power-law creep, showing the shape of the pore. Compaction causes the radius of the curvature of the pore surface to increase from a to a_1.

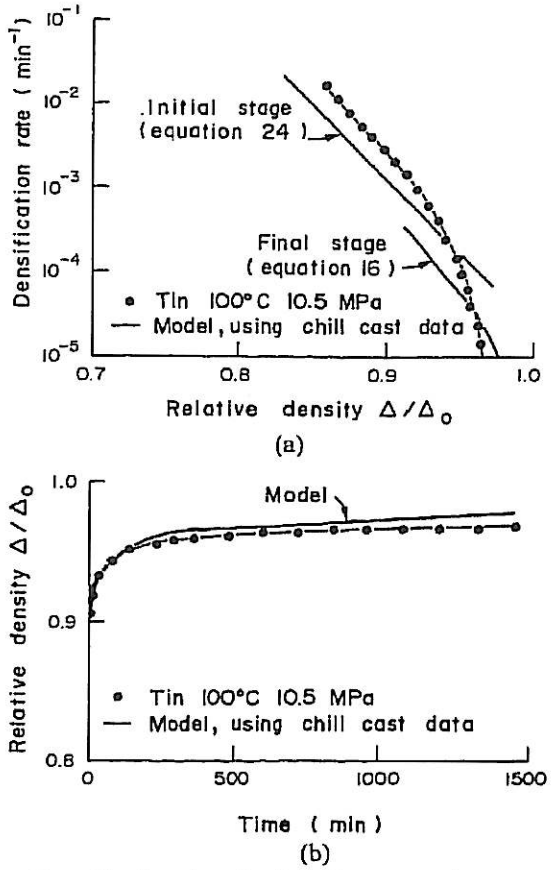

Fig. 25. Densification data for tin when power-law creep is dominant, compared with the new model of Section 6. (a) Densification-rate; (b) density.

comparing the predictions of the model with experimental data an uncertainty lies in the choice of creep data. The hot pressed materials exhibited much lower bulk creep rates than the remelted and chill-cast materials (Figs 16 and 17). By using the data from cast samples, good agreement with the densification data is obtained. The model for pressure sintering by power-law creep then predicts the densification-rates to within a factor of five, and predicts the densities to within 1% of those observed.

Acknowledgements—We wish to thank the S.E.R.C. for their support of the work described in this paper.

REFERENCES

1. P. J. James, *Powder Metall. Int.* **4**, 1 (1972).
2. H. E. Exner, G. Petzow and P. Wellner, *Proc. 3rd Int. Conf. on Sintering and Related Phenomena*, p. 351. Plenum Press, New York.
3. H. F. Fischmeister, E. Arzt and R. L. Olsson, *Powder Metall.* **21**, 179 (1978).
4. C. Torre, *Berg-Hüttenmänn. Monatsh. Montan. Hochschule Leoben* **93**, 62 (1948).
5. A. K. Kakar and A. C. D. Chaklader, *Am. Inst. Min. Engrs. Trans.* **242**, 1117 (1968).
6. A. K. Kakar and A. C. D. Chalkader, *J. appl. Phys.* **39**, 2486 (1968).
7. R. C. Hewitt, W. Wallace and M. C. de Malherbe, *Powder Metall.* **16**, 88 (1973).
8. D. S. Wilkinson and M. F. Ashby, *Proc. 4th Int. Conf. on Sintering and Catalysis*, p. 473. Plenum Press, New York (1975).
9. R. L. Coble, *J. appl. Phys.* **41**, 4798 (1970).
10. A. L. Ramquist, *Powder Metall.* **9**, 1 (1966).
11. H. Pastor, *Rev. Int. Hautes Temp. Refract.* **9**, 251 (1972).
12. R. M. Spriggs and S. K. Dutta, *Sci. Sint.* **6**, 1 (1974).
13. F. B. Swinkels, Ph.D. Thesis, Cambridge Univ. (1980).
14. D. S. Wilkinson, Ph.D. Thesis, Cambridge Univ. (1978).
15. R. H. Pennington, *Introductory Computer Methods and Numerical Analysis*, 2nd edn, p. 445. Macmillan, New York (1971).
16. M. H. Tikkanen and S. Ylasaari, in *Modern Developments in Powder Metallurgy, I, Fundamentals and Methods* (edited by H. H. Hausner), p. 297. Interscience, New York (1966).
17. K. H. Moyer, *Int. J. Powder Metall.* **15**, 33 (1979).
18. R. V. Hill, *The Mathematical Theory of Plasticity*, p. 2540 Clarendon Press, Oxford (1950).
19. R. W. Heckel, *Trans. Am. Inst. Min. Engrs.* **221**, 671 (1961).
20. R. W. Heckel, *Trans. Am. Inst. Min. Engrs.* **221**, 1001 (1961).
21. P. Murray, E. P. Rodgers and J. Williams, *Trans. Br. Ceram. Soc.* **53**, 474 (1954).
22. J. K. MacKenzie and R. Shuttleworth, *Proc. Phys. Soc.* **1362**, 833 (1949).
23. T. Vasilos, *J. Am. Ceram. Soc.* **43**, 517 (1960).
24. J. Williams, in *Symposium on Powder Metallurgy* (edited by Iron and Steel Inst.) (1956).
25. J. D. McClelland, *J. Am. Ceram. Soc.* **44**, 526 (1961).
26. T. Vasilos and R. M. Spriggs, *J. Am. Ceram. Soc.* **46**, 493 (1963).
27. F. E. Westerman and R. G. Carlson, *Trans. Am. Inst. Min. Engrs.* **221**, 649 (1961).
28. F. V. Lenel and C. S. Ansell, in *Modern Developments in Powder Metallurgy* (edited by H. H. Hausner), Vol. 1, p. 281. Plenum Press, New York (1966).
29. J. G. Early, F. V. Lenel and G. S. Ansell, *Trans. Am. Inst. Min. Engrs.* **230**, 1641 (1964).
30. T. Vasilos and R. M. Spriggs, *Prog. Ceram.* **4**, 95 (1966).
31. G. M. Fryer, *Trans. Br. Ceram. Soc.* **66**, 127 (1967).
32. A. G. Atkins, A. Silverio and D. Tabor, *J. Inst. Metals* **94**, 369 (1966).
33. K. L. Johnson, *J. Mech. Phys. Sol.* **18**, 115 (1970).
34. J. R. Matthews, *Acta metall.* **28**, 311 (1980).
35. H. F. Fischmeister and E. Arzt, *Powder Metall.* In press.
36. E. Arzt, *Acta metall.* **30**, 1883 (1982).
37. E. Arzt, M. F. Ashby and K. E. Easterling, *Metall. Trans.* **14A**, 211 (1983).
38. C. L. Vold, M. E. Glicksman, E. W. Kammer and L. C. Cardinal, *J. Phys. Chem. Solids* **38**, 157 (1977).
39. E. W. Kammer, L. C. Cardinal, C. L. Vold and M. E. Glicksman, *J. Phys. Chem. Solids* **33**, 1891 (1972).
40. Th. Huemann and J. Johannisson, *Acta metall.* **20**, 617 (1972).
41. E. B. Greenhill and S. R. McDonald, *Nature* **171**, 37 (1953).
42. J. B. Hudson and R. E. Hoffman, *Trans. Am. Inst. Min. Engrs.* **221**, 761 (1961).
43. N. H. Nachtrieb, *Physics of Solids at High Pressure* (edited by C. T. Tomixuka and R. M. Emrick). p. 336. Academic Press, New York (1965).
44. B. Okkerse, *Acta metall.* **2**, 551 (1954).
45. W. Lange and D. Bergner, *Physica. status solidi.* **2**, 1410 (1962).
46. N. A. Gjostein, *Surfaces and Interfaces* (edited by J. J. Burke, N. L. Reed and V. Weiss), p. 271. Syracuse Univ. Press (1967).
47. S. Dushman and J. M. Lafferty, (editors, *Scientific Foundations of Vacuum Technology* Wiley, New York (1962).
48. J. Weertman, *Trans. Am. Inst. Min. Engrs.* **218**, 217 (1960).
49. J. E. Breen and J. Weertman, *J. Metals*, p. 1230.
50. *Metals Handbook A.S.M.*, Vol. 1, 8th edn. (1961).
51. T. E. Tietz, *Proc. ASTM* **59**, 1052 (1959).
52. *The Properties of Tin.* Tin Res. Inst. Publ. (1954).